Deep convective clouds distribution over the Mediterranean region from AMSU-B/MHS observations

Beatriz M. Funatsu, Jean-François Rysman, Chantal Claud, Jean-Pierre Chaboureau

Atmospheric Research 207 (2018) 122–135

Contents lists available at ScienceDirect

Atmospheric Research

journal homepage: www.elsevier.com/locate/atmosres

Deep convective clouds distribution over the Mediterranean region from AMSU-B/MHS observations

Beatriz M. Funatsu[a,*], Jean-François Rysman[b,d], Chantal Claud[b], Jean-Pierre Chaboureau[c]

[a] CNRS, Université de Nantes, UMR 6554 LETG, Nantes, France
[b] LMD/IPSL, CNRS UMR 8539, École Polytechnique, Université Paris Saclay, ENS, PSL Research University, Sorbonne Universités, UPMC Univ Paris 06, Palaiseau, France
[c] Laboratoire d'Aérologie, Université de Toulouse, CNRS, Toulouse, France
[d] Institute of Atmospheric Sciences and Climate (ISAC), National Research Council (CNR), Rome, Italy

ARTICLE INFO

Keywords:
Convective overshooting
Microwave observations
Mediterranean
Deep convection

ABSTRACT

This study analyses the characteristics and the spatio-temporal distribution of convective overshooting (COV) clouds in the Mediterranean using passive microwave observations from sounders onboard polar-orbiting satellites. COV has distinct microphysical properties that sets them apart within deep convective (DC) clouds, injecting high content of ice in mid to high troposphere (1 g m^{-3} at 8 km in average). The ratio of COV to DC shows largest occurrences over continental Europe during summer (~20% of DC cases), and mostly over the sea and coastal areas in autumn (~13% of DC events). COV frequency presents interannual variation and spatial interannual variability in all seasons. COV preferred location follows a seasonal migration from land in summer to sea and coastal areas in autumn, and also occurs during winter, mostly over the sea. In continental areas the diurnal cycle of COV tends to peak in the afternoon during summer; it is less marked over the sea, yet it shows a slight preference for early morning and afternoon occurrences. The spatial resolution (~20 km) of COV detection makes this database valuable for climatic studies.

1. Introduction

Convective overshooting (COV) clouds are a subset of deep convective (DC) clouds that present a high ice content at high altitude (Rysman et al., 2016a) and are usually diagnosed in the tropical region, where they penetrate the tropopause and play important roles in water vapor regulation in the lower stratosphere (Holton and Gettelman, 2001; Hassim and Lane, 2010; Iwasaki et al., 2010; Dauhut et al., 2015). Such deep convective clouds have the potential to cause extensive damage as they are often connected to heavy rainfall, lightning, hail and tornado occurrence (e.g., Reynolds, 1980; Negri and Adler, 1981; Adler et al., 1985; Altaratz et al., 2003; Brunner et al., 2007; Machado et al., 2009; Bedka, 2011; Petrova et al., 2014; Barthlott et al., 2016; Punge and Kunz, 2016; Kotroni and Lagouvardos, 2008, 2016; Marra et al., 2017).

In general, the development of deep convective clouds in the Mediterranean is associated to a number of physical and dynamical processes that evolve seasonally and are geographically distinct: From autumn to spring, DC clouds in the western part of the basin are mainly linked to the passage of upper-level troughs that propagate from the mid-latitudes and triggers baroclinic instability and cyclogenesis (e.g., Massacand et al., 1998; Jansà et al., 2001; Trigo et al., 2002; Levizzani et al., 2010; Melani et al., 2013; Flaounas et al., 2015; Raveh-Rubin and Wernli, 2015), though meso-scale lows and squall lines have also been linked to severe weather and heavy rainfall (e.g., Turato et al., 2004; Jansà et al., 2001). In the eastern part, precipitation is confined mostly to October through May and associated to the interaction of an upper-level trough in the region and sub-synoptic systems such as Cyprus lows (Altaratz et al., 2003; Saaroni et al., 2010), Red Sea troughs (Kahana et al., 2002; Ziv et al., 2005), and tropical–extratropical interactions in the form of tropical plumes (Rubin et al., 2007), or a combination of these (Dayan et al., 2015). As spring transitions to summer, there is a higher frequency of convective weather systems (outside the eastern Mediterranean) that are mainly thermally forced by the increase in solar radiation, which destabilizes the boundary layer; at the same time the occurrence, timing and location of deep convection are further modulated by the complex topography of the Mediterranean region (including the presence of numerous islands of different sizes). Indeed, several studies have demonstrated the influence of orography on the lighting occurrences and on the diurnal cycle of deep convection

* Corresponding author.
E-mail addresses: beatriz.funatsu@univ-nantes.fr (B.M. Funatsu), jfrysman@lmd.polytechnique.fr (J.-F. Rysman), chantal.claud@lmd.polytechnique.fr (C. Claud), Jean-Pierre.Chaboureau@aero.obs-mip.fr (J.-P. Chaboureau).

https://doi.org/10.1016/j.atmosres.2018.03.003
Received 18 October 2017; Received in revised form 23 February 2018; Accepted 12 March 2018
Available online 13 March 2018

(Altaratz et al., 2003; Barthlott and Kirshbaum, 2013; Barthlott et al., 2016; Kotroni and Lagouvardos, 2008; Mandapaka et al., 2013; Petrova et al., 2014), the persistence of overhooting tops and cold clouds (Bedka, 2011; Levizzani et al., 2010), the propagation of convective systems (Laviola et al., 2011; Levizzani et al., 2010), and intensity and location of cyclone development (Alpert et al., 1999; Trigo et al., 2002; Kotroni et al., 2006; Saaroni et al., 2010; Campins et al., 2011; Cohuet et al., 2011; Raveh-Rubin and Wernli, 2015).

Overshooting tops, lightning and heavy precipitation are commonly used as proxies to identify and characterize intense convection over the Mediterranean region. Overshooting tops (OTs) constitute a proxy for severe weather, consisting of small clusters (< 15 km) within overshooting clouds that typically last < 15 min. OTs are detected using sophisticated image classification techniques applied upon Meteosat infrared imagery (Bedka, 2011). Lightning can be easily detected using ground-based networks (Altaratz et al., 2003; Petrova et al., 2014; Barthlott et al., 2016; Kotroni and Lagouvardos, 2008, 2016). Lightning flashes are the byproduct of strong updrafts, which favor the formation of both graupel and supercooled liquid water at the origin of charge separation. The higher ice content in deep convective clouds is suggested to influence the frequency of lightning activity (Galanaki et al., 2016).

In terms of seasonality, lightning flashes in the eastern Mediterranean winter were found to be more frequent over the sea than over land, while in autumn and spring the flash density is similar above land and sea areas (Altaratz et al., 2003). More OTs were detected over land from April to August, while in September, OT occurrences were mostly found over maritime areas. Concerning extreme precipitation, Nastos et al. (2013) found based on both the Tropical Rainfall Measurement Mission (TRMM) 3B42 product and high resolution ground data that in winter the number of heavy and very heavy precipitation days (exceeding 10 and 20 mm/day, respectively) is larger over the western Mediterranean sea, and over the mountainous coastal areas from the eastern Adriatic to the Levant, and their surrounding seas. In summer, very heavy precipitation days were found essentially over land, with maxima over the Alps. In this season, precipitation and deep convection are virtually absent in the eastern Mediterranean region (e.g., Levizzani et al., 2010; Dayan et al., 2015 and references therein).

The majority of studies on convective systems in the Mediterranean that rely on satellite data are based on measurements provided by infrared or water vapor bands available from geostationary satellites, due to their fine-scale (few km at nadir) and high temporal (~15 min) resolutions. Convective activity detection using these data is achieved by means of sophisticated image classification techniques that permit the discrimination between deep convection and cold cirrus clouds (e.g., Levizzani et al., 2010; Bedka, 2011, Proud, 2015). However, there are a limited number of studies specifically on COV clouds in the region.

In contrast to geostationary satellites, polar-orbiting satellites that carry microwave sounding instruments (such as NOAA and MetOp) overpass the same location on the globe twice daily, thus requiring a number of platforms with distinct equatorial crossing times to have multiple diurnal sampling. Compared to infrared data, microwave has the advantage that it can penetrate non-precipitating clouds and therefore provides three-dimensional information on cloud structure. Passive microwave sounders are able to detect COV as a result of the strong scattering from frozen hydrometeors present in these clouds. Rysman et al. (2016a) documented COV in the Mediterranean using microwave data from the Advanced Microwave Sounding Unit (AMSU) module B during an intensive observation campaign for the HyMeX project (SOP-1; 5 September to 6 November 2012). They used a method first proposed by Hong et al. (2005) for the tropical region, in which a differential relationship between water vapor sensing channels of AMSU is used for COV detection. They found based on two case studies that COV had high ice content up to 12.5 km in altitude and was associated with heavy concentration of frozen hydrometeors reaching 1.5 g m^{-3} in the middle-to-upper troposphere. Furthermore, it was found that during the two months under scrutiny COV occurred in 0.3‰ of the total observation time. This study was later expanded by Rysman et al. (2016b) where they presented an evaluation for rainfall and deep convection of a regional climate model using AMSU-based diagnostics through a model-to-satellite approach (Chaboureau et al., 2012; Matsui et al., 2014). They showed that simulated BTs are overall higher than observed BTs in convective regions because the studied model produced too few frozen hydrometeors. Subsequently Rysman et al. (2017) used 10-year CloudSat radar and CALIPSO lidar data to retrieve ice cloud properties (Delanoë and Hogan, 2008, 2010), and NOAA-18's MHS data to assess and characterize DC and COV for the area 60°S–60°N. They showed that in COV clouds ice water loading and maximum height are larger than for DC clouds without overshooting. However, the specific properties of convection in the Mediterranean area were not assessed. This is an important point as such differentiation in ice content seems to have an important effect on the simulation of severe storms in the Mediterranean (Rysman et al., 2016b), and could be related to the occurrence of lightning activity (Galanaki et al., 2016).

Although a direct link between COV and a particular intensity of high-impact weather proxies has not been established, the study of COV as a particular class of deep convective clouds is warranted: distinctive microphysical characteristics with a larger ice water content at higher altitudes can impact lightning occurrence and/or graupel formation, and have the potential to change the upper-tropospheric and lower stratospheric water vapor distributions. Thus, in this work a characterization of convective properties, frequency and distributions of COV and DC in the Mediterranean region is presented. Comparisons between COV and DC frequency and distribution are also investigated, as this proportion is still largely unknown in the Mediterranean. Seasonal COV frequencies over the Mediterranean using AMSU-B/MHS onboard several NOAA and MetOp platforms were examined to determine whether COV occurs year long, and where, as well as whether there are preferential seasons and locations. Finally the diurnal distribution of COV occurrences throughout the day is examined by taking advantage of AMSU-B in multiple platforms that sample in distinct time windows. Studying the diurnal cycle is fundamental to test our knowledge of small and large-scale interactions, cloud microphysics, and air-sea-land interactions; this is particularly crucial in the Mediterranean region where land-sea contrasts and topography are key features that complicate the prediction of intense events.

The direct, simple methodology developed by Hong et al. (2005) – and assessed by Rysman et al. (2016a) in the Mediterranean and Rysman et al. (2017) at near-global scale – is applied in order to detect and characterize COV activity. The layout of the article is as follow: Section 2 describes AMSU data and their known issues, the method applied to detect deep convective clouds and perform the cloud microphysics characterization. Sections 3 and 4 group the main results, with a first part (Section 3) centered on the differences between COV and DC, and a second part addressing the COV spatio-temporal distributions. Specifically, Section 3 lays out a microphysical characterization of COV that confirms that COV is a distinctive subset of DC in the Mediterranean. A comparison of the spatio-temporal distributions of COV relative to that of DC is also presented in this section. Section 4 focuses on the COV spatio-temporal variability, in diurnal, seasonal and annual scales. Finally, Section 5 presents the summary and main conclusions of our study.

2. Data and methods

2.1. AMSU instrument

AMSU is a cross-track scanning microwave-based sounder operating onboard NOAA and MetOp polar-orbiting platforms since late 1998. Details of the instrument, calibration and known issues can be found in the NOAA KLM User's guide (available at http://www.ncdc.noaa.gov/

oa/pod-guide/ncdc/docs/klm/index.htm), and in Bennartz (2000), Goldberg et al. (2001), Funatsu et al. (2007), Surussawadee and Staelin (2010), Claud et al. (2012), John et al. (2013), Chung et al. (2013).

The AMSU instrument has two modules, A and B, designed to provide optimal vertical sampling information on temperature and water vapor, respectively. Both modules have swath width of approximately 2300 km. AMSU-B cross-track consists of 90 steps spanning 48° to each side of nadir, with the step angle between two earth views of 1.1°. The horizontal resolution varies from ~16 km at the near-nadir positions, degrading to 27 × 54 km at the furthest field-of-view. In the present study we use only data from AMSU-B, which has 5 channels: 2 window channels (channel 1 at 89 GHz and channel 2 at 150 GHz; not exploited here), and 3 humidity sounding channels (channels 3–5, centered around 183.3 GHz: channel 3 at 183.3 ± 1, channel 4 at 183.3 ± 3, and channel 5 at 183.3 ± 7 GHz). Starting from NOAA-18 the AMSU-B module was replaced by the Microwave Humidity Sounder (MHS), which has slightly different sampling frequencies (channels 2 operates at 157 GHz in MHS, while channel 5 operates at 190 GHz in MHS) but that does not significantly affect the detection of precipitation and deep convection using the method used in this study (described below) as indicated by Claud et al. (2012). Hereafter the term AMSU-B will be used to denote both AMSU-B and MHS instruments. NOAA-XX platforms will be designated by NXX, where XX is the platform number (for example, N18 for NOAA-18), and MetOp platforms will be designated as M02 for MetOp-A and M01 for MetOp-B.

The equatorial crossing local time for each platform from 1999 to 2014 is shown in Fig. 1 (afternoon (PM) and morning (AM) for ascending/descending nodes), and Table 1 indicate the launch dates and reported issues for channels 3–5 of AMSU-B/MHS. The maximum diurnal coverage corresponds to the period of 2005–2007: In 2005 N15–N18 (N18 was launched in May 2005) were active, while M02 was launched in October 2006. After 2009 AMSU-B/MHS on several platforms presented problems, and at present (2017) only N18, M02 and M01 provide functional MHS data. A new MetOp (MetOp-C) platform is scheduled for launch in 2018.

AMSU asymmetry problems were detected for both AMSU-A (Weng et al., 2003) and –B/MHS (Buehler et al., 2005; John et al., 2013) modules. Scan asymmetries refer to the differences measured by one side of the scan track relative to the equivalent scan position on the other side of the track (e.g., position 1 and position 90, or position 2 and position 89, etc.), for the same target. The issue of scan asymmetries is particularly complex because bias (i) are platform dependent, (ii) are scan side/position dependent, (ii) vary with the humidity sounder channel, and (iv) vary with time. Buehler et al. (2005) found large scan asymmetries for N15, while for N16 and N17 the asymmetries were small, comparable to the instrument noise. Subsequently, John et al. (2013) found that the asymmetries vary for different platforms, channels, and with time. Channels 3–5 of N15 and N16 were found to have larger scan-dependent bias compared to N17, particularly after 2006. Furthermore, residual uncorrected radio-frequency

Table 1
Launch dates of NOAA (N15 - N19) and MetOp (M02, M01) platforms carrying either AMSU-B (N15-N17) or MHS (N18, N19, M02, M01), and reported issues.

N15	[13-May-1998] Launch [20-May-1998] Gradient bias observed due to interference from STX1 (radio interference). [03-Nov-1998] Gradient bias no longer present due to STX1 deactivation. [Apr–Aug/2003] Intermittent (≤24 h) AMSU-B scan motor current and component temperature surge. [2006–2010] important scan asymmetries varying with time (John et al., 2013). [14-Sep-2010] Signal degraded due to failed Channel 3–5 Oscillator. [16-Sep-2010] Channels 3–5 turned off. [20-Sep-2010] Channels 3–5 local oscillator failed; channels 3–5 failed.
N16	[21-Sep-2000] Launch • Significant asymmetry problems in channels 3–5 detected after 2006 • Platform decommissioned in 2014
N17	[24-Jun-2002] Launch [20-Aug-2003] Intermittent elevated (50%) noise levels detected in channels 3 and 4 (no report if only for this day or continued). [2006–2010] important scan asymmetries varying with time (John et al., 2013); residual uncorrected radio-frequency interference detected (Surussawadee and Staelin, 2010). [16-Dec-2009] Channel 3–5 Local Oscillator Failed. Science Data from Channel 3–5 are degraded. [13-Jan-2010] Channel 3–5 permanently failed. • Platform decommissioned in 2013
N18	[20-May-2005] Launch • Since April 2009 there have been several intermittent glitches on the MHS instrument and corrections or adjustments have been made. Data should be used with caution, particularly after 2014.
N19	[11-Feb-2009] Launch. [24-Apr-2009] MHS entered spin mode, followed by fault mode. [22-Jun-2009] Channels 3 and 4 noisy. [27-Aug-2009] Continued channels 3 and 4 degradation has rendered the MHS data unusable for various user products.
M02	[19-Oct-2006] Launch • MHS exhibits some problems since 26 March 2014.
M01	[17-Sep-2012] Launch

Sources: https://www.wmo-sat.info/oscar/satellites, http://www.ospo.noaa.gov/Operations/POES/status.html (accessed on 27-Dec-2017).

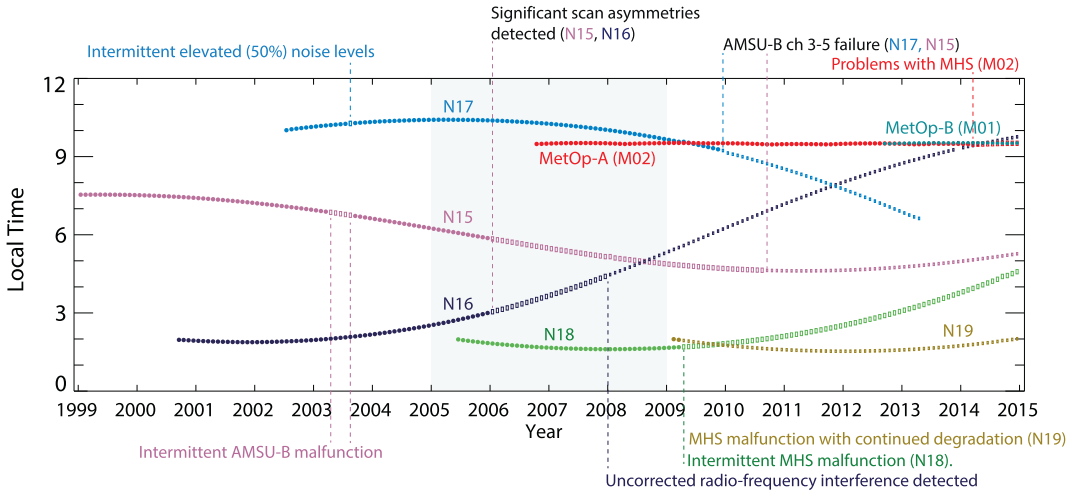

Fig. 1. Equatorial crossing time (local time) for the ascending (afternoon)/descending (morning) nodes of NOAA and MetOp platforms for the period 1999–2014 (source: http://www.ospo.noaa.gov/Products/ppp/navpage.html). Open symbols denote periods where problems with AMSU-B or MHS were reported (see Table 1 for extended report for each platform). The period of 2005–2008, with a maximum temporal coverage, is shadowed.

interference was detected in N16 data (Surussawadee and Staelin, 2010). Only MHS instruments onboard N18 and M02 were found to have small scan-dependent bias.

Laviola et al. (2013) evaluated the impact of scan asymmetries of N15 and N16 on rainfall retrievals based AMSU-B/MHS water vapor channels for January and February 2006. They found that the scan-dependent bias - even those as large as those reported by John et al. (2013) - did not translate to a significant asymmetry in rain retrievals. They attributed these findings to the fact that their retrieval algorithm is based on differences of channels 3–5, limiting the impact of the asymmetries on the results. In the present study we did not apply a scan-dependent bias correction to the data. We discarded data from N16 after 2007 due to both scan asymmetries and radio interference data, and considered only the period of 2005–2008 for the analysis of spatial and diurnal variability of COV, however it includes N15 data for the period of 2007–2008. Microphysical properties of COV data were studied using only N18 MHS data, and thus, minimizing scan-dependent bias effects.

2.2. Detection of COV and DC

The detection of convective overshooting and deep convection was performed using a combination of the humidity sounding channels of AMSU-B, i.e., channels 3 to 5. Microwave radiation in these high-frequency channels is affected by emission by liquid hydrometeors and scattering by frozen hydrometeors. Deep convective clouds are characterized by higher contents of high density frozen hydrometeors (graupel or hail) carried at higher levels in the convective core contributing to the brightness temperature depression found at higher frequencies. The brightness temperature depression is higher as channel frequencies are further away from the center frequency at 183.3 GHz. These observations led Hong et al. (2005) to propose criteria to detect DC and COV in the tropical region based on the difference between humidity-based channels: Deep convective clouds satisfy simultaneously the condition: $B3m5 \geq T_0$ (B3m5 corresponding to the difference between the brightness temperatures of channels 3 and 5) and $B3m4 \geq T_0$ and $B4m5 \geq T_0$, whereas COV obey the order relation $B3m5 \geq B3m4 \geq B4m5 > T_1$. Notice that the COV criterion satisfies the DC one, and COV is therefore a subset of DC. In the Mediterranean, DC was found to correspond well with areas of heavy precipitation when compared to Tropical Rainfall Measuring Mission (TRMM) 3B42 product and ground-based data (Funatsu et al., 2007).

Scan positions further away from the nadir (center fields of view) sound a thicker layer of the atmosphere, thus affecting the measured brightness temperature (Goldberg et al., 2001; Greenwald and Christopher, 2002). For AMSU-B high frequency channels Greenwald and Christopher (2002) have shown that the limb effect causes a depression smaller than 1 K for the inner ~40 positions, increasing to 5 K at the edges. Since the DC and COV detecting thresholds proposed by Hong et al. (2005) rely on differences between channels, it is assumed that the limb effect does not strongly influence the detection result. Another issue inherent to scan-track measurements is that at the edge of the scan the spatial scale difference between the convective core (or overshooting region) and the instantaneous field of view size might have a significant impact on the signal related to COV or DC. Such effect has not been assessed here. In this study, as in Funatsu et al. (2009), the original brightness temperature data were first interpolated to a $0.2^\circ \times 0.2^\circ$ regular latitude × longitude grid. In the northern part of the Mediterranean region the brightness temperatures of different orbits were averaged in regions where these orbits overlap. This approach provides twice daily brightness temperature for each channel and each platform, however the information on the scan position is lost as the interpolation weights in only the distance of the measurement to the regular grid. The regridding of the data means that thresholds for DC and COV fixed according to the viewing angle, as originally proposed by Hong et al. (2005), cannot be applied. For DC, we fixed $T_0 = 0$ K, as done by Funatsu et al. (2007) who showed that DC identified using the same methodology detects heavy precipitation in at least 50% of cases when compared to 3-h TRMM 3B42 (v6) data. For COV, Rysman et al. (2017) found that the percentage of false positives has little variation with the viewing angle up to 45°. We fixed $T_1 = 0$ K, i.e., all grid points in the regridded data were assumed to carry little effect of the viewing angle. After regridding the data, a flag for DC or COV occurrence was assigned for each grid point. Finally, the number of DC or COV occurrences for each hour was re-sampled to a $1^\circ \times 1^\circ$ grid, and the number of valid grid points (i.e., grid points with an actual measurement) was retained. The results were then aggregated to form monthly means, that is, all COV occurrences are first summed, then divided by the number of days in the month and by the number of years and by the number of valid grid points. For the diurnal analysis, the average was done by fixing the hour, and dividing by the number of years, months, and valid grid points. The target domain corresponds to the area comprised between 28°–48°N and 10°W–40°E, the sea flag in the calculations considers only the Mediterranean Sea, and coastal areas were flagged as land.

Rysman et al. (2017) found that the DC criterion yields many false positives between October and April in high latitudes when the surface is frozen, as well in high, mountainous regions for the same reason. Under dry conditions, the cold surface contaminates the brightness temperature measured by the water vapor channels of AMSU-B. They found however that detection of COV was not severely affected. An assessment of the uncertainty due to the possible contamination of the brightness temperature by the cold surface under clear sky conditions was performed here for the Mediterranean region. First, for each year and month of the period (2005–2008) the orbits of available satellites overpassing the Mediterranean were scanned. Then a list was derived with all locations in which DC or COV were detected (no regridding was performed for this assessment), along with an estimation of the upper tropospheric humidity with respect to ice (UTHi), as proposed by Buehler et al. (2008). Then, the European Centre for Medium-Range Weather Forecasts ERA-I Reanalysis (Dee et al., 2011) snow depth and skin temperature data, along with UTHi, were used to screen out all points that had snow depth > 1 cm or skin temperature < -2°C (for the nearest gridpoint, nearest hour), and with UTHi $< 65\%$. Only the inner 54 scan positions were screened, as they are less affected by the limb effect. This screening showed that in January and February the average rate of false positives for DC is high, reaching above 50%, while for COV it remains relatively low, at most ~7% in February. False positives are still significant for DC in December (~37%), much fewer for March (~27%), but negligible for COV (~3% and < 2%, respectively). The results are summarized in Table 2. The false positives for DC (COV) occur predominantly over high topography: 77.7% (99.3%) for height > 1 km, 56.5% (89.0%) for height > 1.5 km, and 38.3% (62.8%) for height > 1.8 km. Only 18.7% (0.7%) false positives were detected for elevation < 500 m. Given the elevated number of false positives in winter, analyses including DC were performed for March to November only.

Table 2
Proportion of false positives for DC and COV over the period 2005–2008. False positives were considered when ERA-I snow depth > 1 cm or skin temperature < 271 K and upper tropospheric humidity with respect to ice < 65%. See text (Section 2.2) for details.

	DC (%)	COV(%)
January	53.4	2.5
February	51.6	6.3
March	26.5	1.6
April	2.6	0
May	0.05	0
October	0.3	0
November	7.5	0.4
December	36.6	3.4

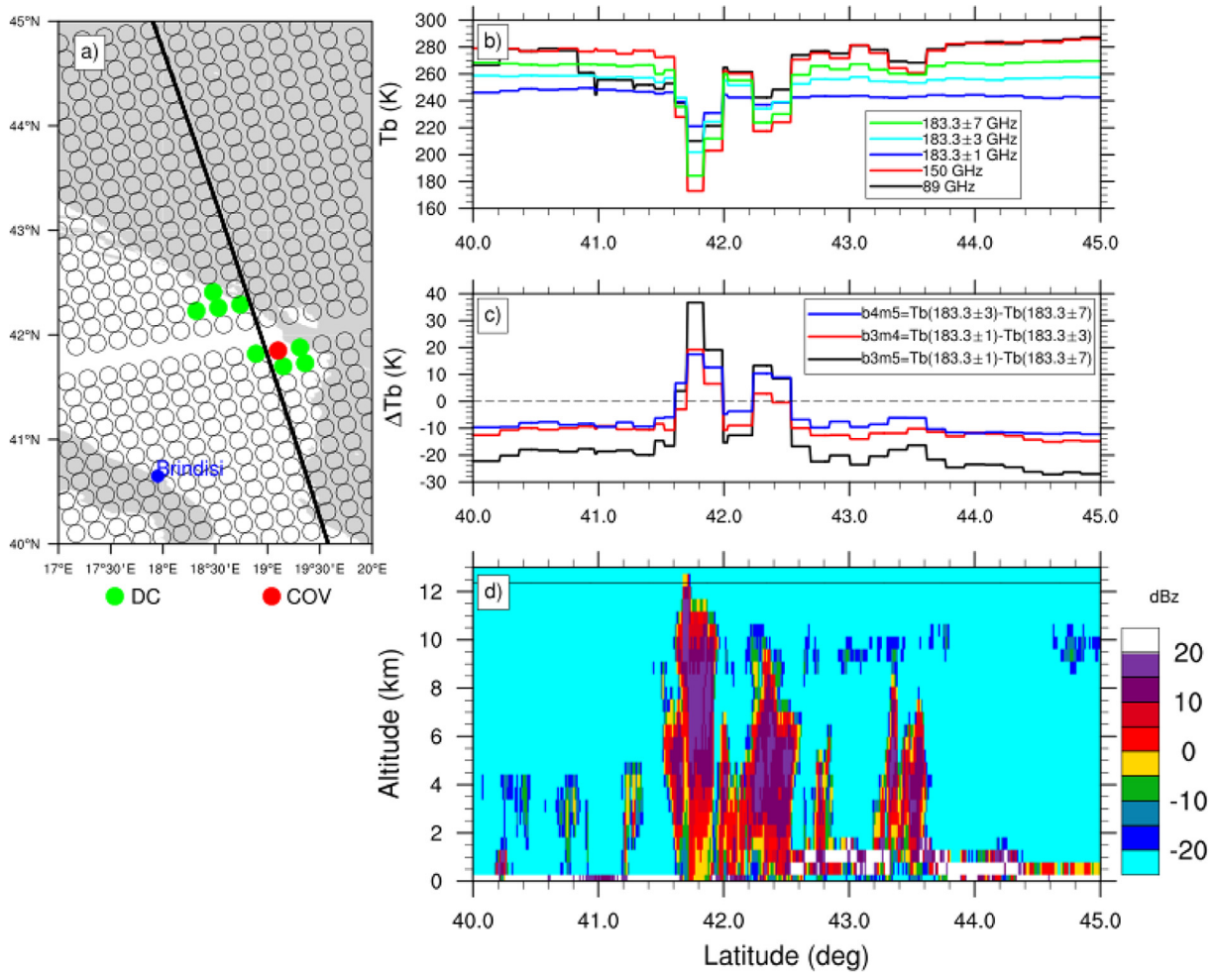

Fig. 2. (a) Deep convective (DC; green) and convective overshooting (COV; red) clouds detected by MHS on NOAA-18 for 12 UTC 17 September 2009. Open circles correspond to AMSU measurements without neither DC nor COV. Shaded areas correspond to land, white to the Adriatic Sea. The location of Brindisi (rawinsonde site) is marked in blue. Dark line corresponds to the cross section along which profiles for panels (b)–(d) are shown: (b) Brightness temperature of MHS channels 1–5 (1: 89 GHz, 2: 150 GHz, 3: 183 ± 1 GHz, 4: 183 ± 3 GHz, 5: 183 ± 7 GHz); (c) Brightness temperature differences between humidity channels (3–5); (d) CloudSat Cloud Profiling Radar reflectivity as a function of altitude. NOAA-18 and CloudSat overpassed the convective overshoot at 1207 UTC and 1202 UTC, respectively. In (d) the line shown at 12.345 km is the altitude of the cold point tropopause temperature (−57.9 °C) as recorded by the radiosonde launched from Brindisi, Italy, at 1200 UTC 17 September 2009. (For interpretation of the references to colour in this figure legend, the reader is referred to the web version of this article.)

An example of COV occurrence in the Mediterranean basin is illustrated in Fig. 2, for an intensive convective event that occurred on the 17 September 2009 that was observed both by N18 MHS and the CloudSat Cloud Profiling Radar. The left-hand panel (Fig. 2a) shows DC (green) and COV (red) occurrences at 1200 UTC at the southern tip of the Adriatic Sea near 42°N, 18°–19.5°E. A cross section through the area shows that there was a strong depression in the brightness temperature at all MHS channels (Fig. 2b), indicating large scattering by hydrometeors. Fig. 2c indicates that the cluster near 42°N present brightness temperature differences that are equal or greater than zero, indicating the presence of deep convection. Specifically, COV condition is satisfied near 42°N, while vertical cross section of reflectivity obtained from the CloudSat Cloud Profiling Radar (Fig. 2d) shows that this cluster penetrates well above 10 km, i.e., reaching across the tropopause. This example clearly illustrates the interest of Hong et al. (2005) criteria to identify DC and COV occurrences in the Mediterranean region.

2.3. Microphysical characterization using the DARDAR_Cloud and 2B-CLDCLASS products

The microphysical characterization of COV clouds was conducted by crossing N18 MHS-derived DC and COV detection with information from the DARDAR-Cloud (Delanoë and Hogan, 2008, 2010) and the Cloudsat Level 2 Cloud Scenario Classification (2B-CLDCLASS; Sassen and Wang, 2008) products. The period used for this analysis was 2006–2015.

The 2B-CLDCLASS product corresponds to a cloud classification using Cloudsat radar measurements. The vertical resolution is of about 240 m, and the horizontal resolution may vary between 1 and 25 km. 2B-CLDCLASS classifies clouds into several stratiform and convective categories, including deep convective (cumulonimbus) or high (cirrus and cirrostratus) clouds, based on different rules for hydrometeor vertical and horizontal scales, the maximum effective radar reflectivity factor measured by the cloud profiling radar, indications of precipitation, and other ancillary data. The liDAR + raDAR (DARDAR)-Cloud consists of ice cloud retrieval products derived from the combination of the CloudSat radar and the CALIPSO lidar measurements. Only a brief outline of the product is presented here; the reader is referred to Delanoë and Hogan (2008, 2010) for details. Ice cloud retrievals are available at CloudSat horizontal resolution (1.4 km) and CALIPSO vertical resolution (60 m). The retrieval algorithm uses a variational method for retrieving profiles of visible extinction coefficient, ice water content and effective radius in ice clouds using the combination of radar reflectivity and lidar attenuated backscatter. The retrieved ice water content represents the integrated (ice) particle mass across the size distribution, while the effective radius is a measure of the particle

size, proportional to the ratio of ice water content to visible extinction coefficient. The DARDAR product also archives the tropopause height provided by the Goddard Earth Observing System (Version 5).

As in Rysman et al. (2017), two subsets of deep convective clouds detected by the Hong et al. (2005) method were considered: DC without COV (i.e., grid points that satisfy DC criterion but not the COV one) and COV clouds (which necessarily satisfy the DC criterion). Notice that this differentiation between DC with and without COV was made only for the analysis presented in Section 3. Collocated and coincident measurements of Cloudsat/CALIPSO with N18 were then identified and the DARDAR-Cloud and 2B-CLDCLASS products were extracted for each DC and COV event detected. Only measurements within 15 min apart were considered, and the DARDAR-Cloud profiles were averaged over a pixel of 16 × 16 km^2, corresponding to the MHS resolution at nadir. The DC diagnostic was matched to the corresponding vertical section of atmosphere in the 2B-CLDCLASS product classified as a Deep Convective Cloud (DCC). The COV diagnostic was matched to DCC classification and with the further condition that DARDAR-Cloud ice water content detected in the same vertical section of the atmosphere reaches or overpasses the tropopause.

3. COV: a distinctive subset of DC over the Mediterranean

3.1. Microphysical characteristics

Fig. 3 shows the median vertical distribution and its interquartile range of ice water content (Fig. 3a) and effective radius of hydrometeors (Fig. 3b) based on DC and COV events specifically in the Mediterranean Basin. As laid out in Section 2.3, for this analysis the DC cases considered did not count those with simultaneous COV occurrence so that the results highlight the differences between the two types of deep convective clouds. The median values of ice water content reach around 0.9 g m^{-3} for COV clouds and a little less (~0.8 g m^{-3}) for DC tops (Fig. 3a), but the largest ice water density is found at higher levels for COV clouds (median of 9 km) than for DC clouds (median of 6 km). Moreover COV has a larger range of effective radius of large frozen hydrometeors than DC (without COV) clouds. High values of average effective radius of frozen hydrometeors (> 70 μm) are shown up to 12 km for COV (< 10 km for DC; Fig. 3b). This result suggests a dependence of the BT depression on the particle size through the scattering coefficient. At equal concentration, it is indeed expected that the bigger the particle size, the larger probability of a stronger BT depression.

Rysman et al. (2017) have demonstrated that 51% of detected COV events detected within 60°S–60°N are associated with cloud ice that effectively reached the tropopause, while in 82.1% of the cases the associated cloud ice reached an altitude of < 2 km below the tropopause. Specifically for the Mediterranean region, analysis of the ice cloud height vs tropopause height between 2006 and 2015 (when there were coincident observations of Cloudsat and MHS; not shown) indicated that 12 out of 18 (~67%) detected COV cases using the above criterion cross the tropopause, while 78% (83%) are < 1 km (< 2 km) from the tropopause. These results indicate that the clouds detected using Hong et al. (2005) using COV criterion effectively overshot in most of the cases in the Mediterranean.

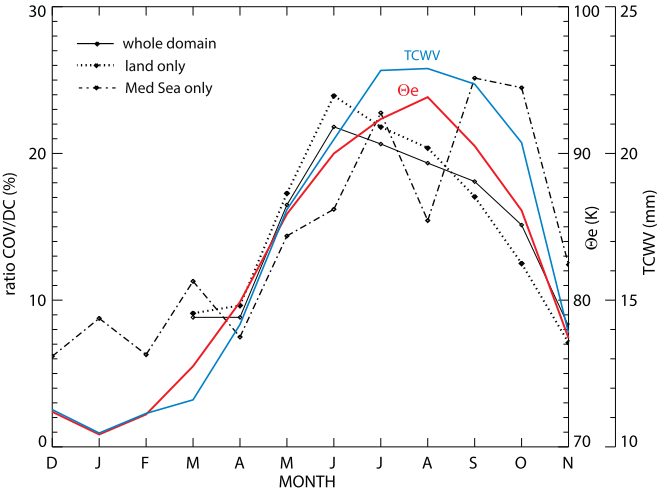

Fig. 4. Monthly mean ratio of COV to DC occurrences for the whole domain, land only, or sea only, for the period 2005–2008. Superimposed is the ERA-I mean equivalent potential temperature difference ($\Delta\Theta_e$) between the 1000 and 300 hPa levels (red) and mean total column water vapor (blue) for the whole domain and same period. (For interpretation of the references to colour in this figure legend, the reader is referred to the web version of this article.)

3.2. Monthly and seasonal COV to DC frequency ratio

The monthly evolution of COV/DC (Fig. 4) shows that spring and autumn are transition seasons, with variations from 10 to 15%, and from 20 to 10%, respectively. This figure also emphasizes the maximum of COV/DC over the sea. The seasonal evolution follows roughly the seasonal evolution of the precipitable water derived from the ERA-I reanalysis, and that of the difference of equivalent potential temperature ($\Delta\Theta_e$) between 1000 and 300 hPa, which is a measure of the convective instability of the air column (the larger the value, the more conditionally unstable). This suggests that the supply of precipitable water and stronger conditionally unstable conditions are underlying factors that promote overshooting occurrence within deep convective clouds. Strong convective instability means that there is a higher chance to carry hydrometeors further up the atmosphere, which is consistent with the vertical profiles of higher hydrometeor content and vertical reach for COVs (than for DC) as shown in Fig. 3.

The seasonal proportion of COV relative to DC is shown in Fig. 5a–c (spring to autumn). The COV/DC ratio shows strong seasonal variation, with the median values increasing from around 12% in MAM to 21% in JJA, and decreasing to 14% in SON. In JJA the ratio COV/DC is relatively homogeneous across the European continent, with values ranging between 13 and 30%, and with some higher values south of the

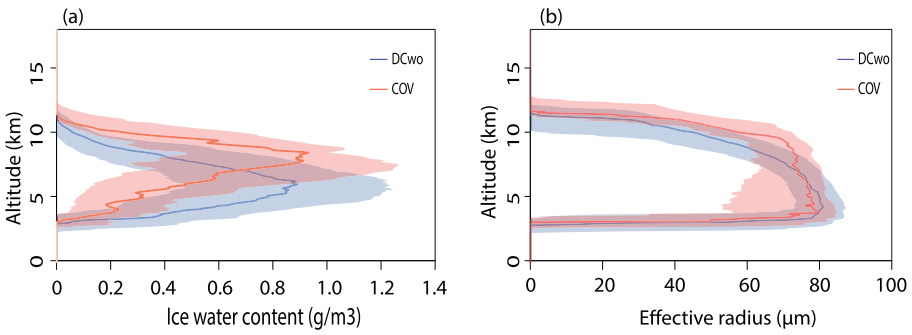

Fig. 3. (a) Median vertical profile of ice water content and (b) median vertical profile of effective radius for DC without overshooting clouds (DCwo; blue) and COV (red). The interquartile range is shown as shaded regions. The period concerned was 2006–2015. (For interpretation of the references to colour in this figure legend, the reader is referred to the web version of this article.)

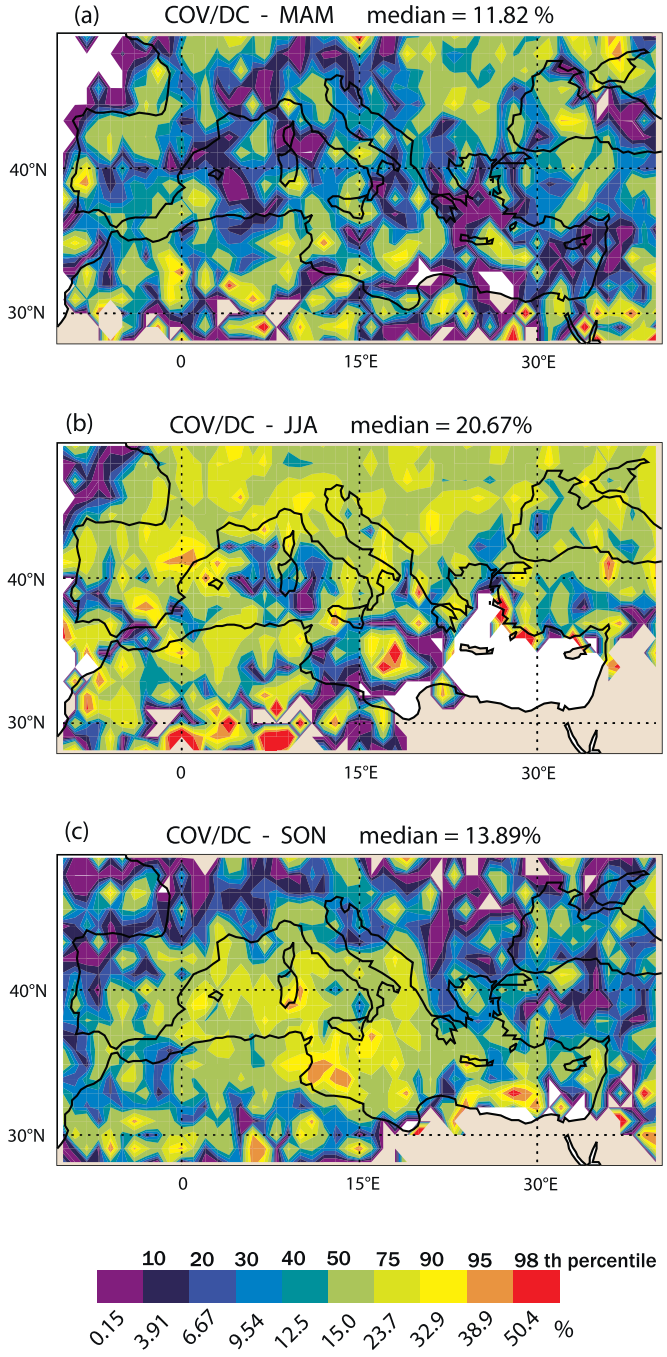

Fig. 5. Ratio of COV to DC occurrences by season (2005–2008): (a) MAM, (b) JJA, and (c) SON. The colour scale classes were fixed according to each COV/DC percentile rank.

Pyrenees, coastal areas of Greece and Turkey, and a large area at the south of Italy. In SON the larger values of COV/DC are spread across the Mediterranean Sea (Fig. 5c).

4. Analysis of COV variability

4.1. Seasonal spatial variability

The spatial distribution of COV by season is presented in Fig. 6a–d. COV was found to occur in all seasons, including in wintertime when COV was detected mostly over the sea and coastal areas, and with few occurrences over land (Fig. 6a). This finding is in agreement with previous studies that found the predominance of lightning activity (another proxy for deep convective activity) over the sea during winter (Holt et al., 2001; Christian et al., 2003; Kotroni and Lagouvardos, 2016). The largest frequencies (up to 0.7‰) are found between Sardinia and Tunisia, around Apulia region in southern Italy (~40.8° N, 17.1° E), and along the Turkish coast. In winter, COV can occur by result of synoptic system forcing that triggers the atmospheric instability. If the sea surface temperature is relatively warm, it can provide enough moisture to support localized convection (Funatsu et al., 2009; Kotroni and Lagouvardos, 2016). In MAM, the frequency range is comparable to DJF (up to 0.7‰, except for a few points where frequency reaches 1‰) however the spatial distribution of COV is rather homogeneous over both land and sea (Fig. 6b) with slight preference for land occurrence (Atlas Mountains, Hungary, Romania, south of Black Sea).

In most of the Mediterranean region, COV occurrences are larger in summer and autumn than in winter and spring months, when frequencies can reach > 1.3‰. Their median frequencies are comparable (0.12‰ in JJA and 0.14‰ in SON), but the dichotomy land (JJA; Fig. 6c) - sea (SON; Fig. 6d) is very marked. Indeed, 50% or more of all occurrences in this period were found over land in summer, and over the sea and coastal areas in autumn. However, in the eastern and southeastern Mediterranean, COV is nearly absent in summer both over land and sea (Fig. 6c), with the exception of a few occurrences in the Levant area. This is because, in general, in the eastern and southeastern Mediterranean precipitation is confined between October–May, with two-thirds within the winter months (December–February), and is dominantly associated with upper-level troughs that interact with surface cyclones, both of which are rarely present in the region in summer (Ziv et al., 2006; Dayan et al., 2015; Funatsu et al., 2009; Raveh-Rubin and Wernli, 2015). In JJA, the largest frequencies were found near the Pyrenees, the Alps, and continental Eastern Europe (outside the Mediterranean influence), suggesting that topography and land thermal effects are determining on the occurrence of COVs. In SON, COV occurred over all the northern and southwestern Mediterranean coastal areas, and over the sea except coastal Egypt. Frequencies above the 90th percentile (1‰) are found over the western Mediterranean Sea, the coast of Turkey, and forming an arc around the Italian peninsula.

The spatial distribution of COV in summer and autumn (Fig. 6c, d) show remarkable agreement with the overshooting tops observed by Bedka (2011) using geostationary data for extended summer (April to September): peak frequencies are found near the Pyrenees, the Atlas range, the Alps, and over continental eastern Europe in summer, and mostly over the sea in autumn. The spatial frequency of COV follows the pattern of "displacement" from land in summer to the sea in autumn that was also detected for other proxies of severe weather events (Bedka, 2011; Alhammoud et al., 2014; Funatsu et al., 2009; Holt et al., 2001; Christian et al., 2003; Kotroni and Lagouvardos, 2016). The spatial distribution of COV/DC (Fig. 5) also follows the seasonal migration with maxima over land in summer (Fig. 5b) and maxima over the sea and coastal areas in autumn (Fig. 5c), and with less preferential sea/land occurrence in spring (Fig. 5a). However, the ratio COV/DC is higher south of that of COV.

The spatial distribution of COV in the Mediterranean region presented above shows a good agreement with results of Nastos et al. (2013). Their study show that over the Mediterranean region, the number of extremely wet days (defined as the number of days exceeding the 99th percentile) and the number of very heavy precipitation days (exceeding 20 mm/day) in winter are located mainly over the western Mediterranean Sea, the Dinaric Alps, mountainous western Greece, coast of Turkey, the Levant region, and their surrounding sea areas, while in summer numbers are larger over continental Europe mainly over elevated areas and away from coastal areas. Some discrepancies between COV and extreme precipitation distributions arise partly because the relationship between brightness temperature and precipitation amounts is not linear (e.g., Funatsu et al., 2007). In addition, because the TRMM 3B42 is a precipitation product that does not

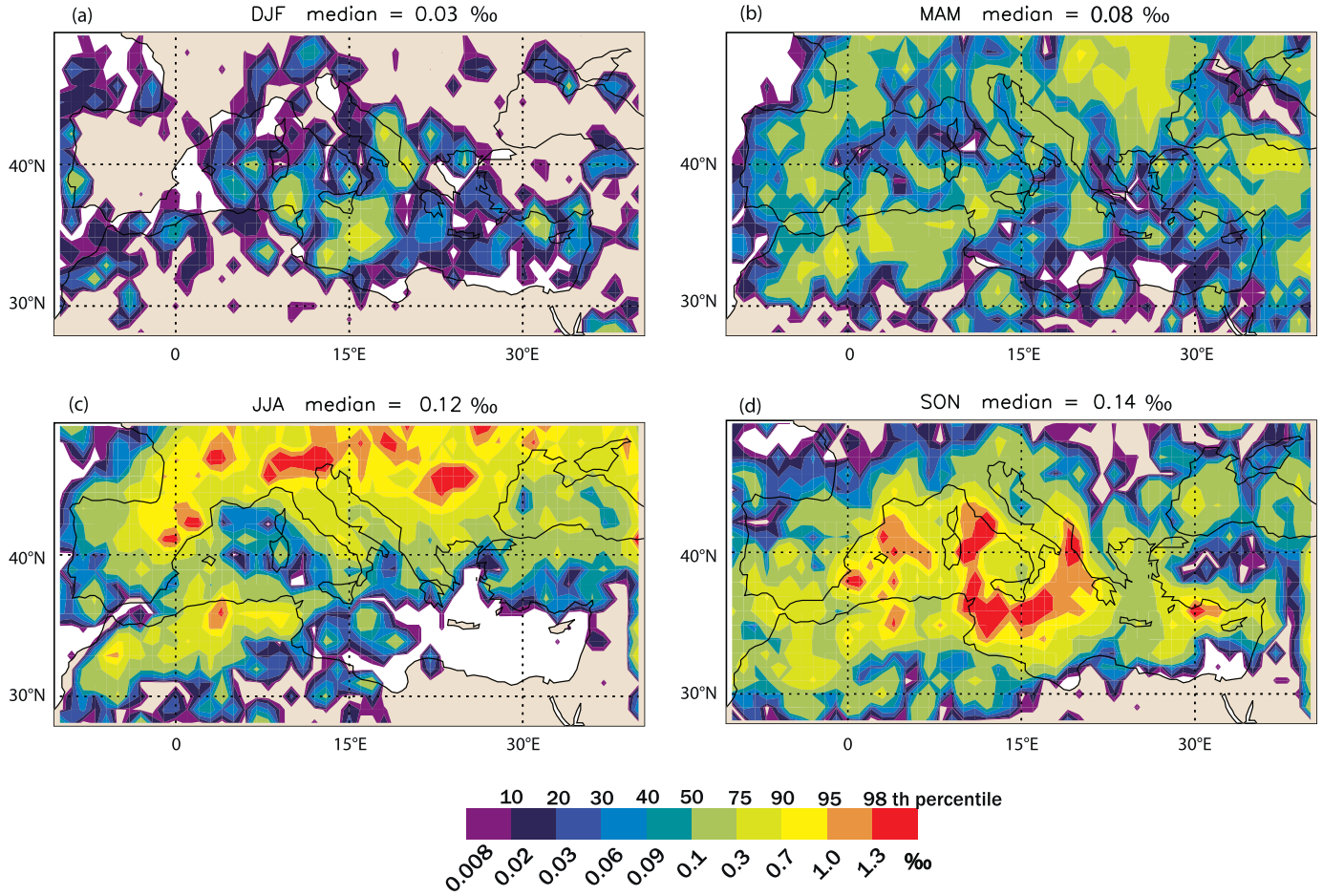

Fig. 6. Frequency of COV (‰) by season averaged over the period of 2005–2008: (a) December–January–February (DJF), (b) March–April–May (MAM), (c) June–July–August (JJA), (d) September–October–November (SON). The relative frequency refers to the occurrences of COV relative to the total number of overpasses over the period. The colour scale classes were fixed according to each COV percentile rank.

discriminate between convective and non-convective precipitation it is not possible to extricate these two categories.

4.2. Interannual variability

Fig. 7 shows the monthly mean time series of COV frequency averaged for all satellites over the domain for the period 2001–2014 (black), and its standard deviation (shadowed). For each satellite, the monthly mean COV frequency was computed by dividing the total number of COV grid points by the number of valid grid points (i.e., grid points with a BT measurement) in the month. Then, an average for all satellites was performed, thus taking in account the number of satellites (as shown in the horizontal bars at the top of the figure). Fig. 7 shows a marked seasonal cycle that has strong interannual variability. Part of the interannual variability is due to the uneven number of satellites throughout the period, and the different equatorial crossing times thus sampling different times of the day. However, these factors do not explain all the variability as distinct patterns can be seen for example during 2003–2005 (2014–2015), when N15-N17 (N18, M01, M02) were active and these platforms did not considerably drift (thus sampling nearly the same time of the day during the period). The time series of monthly mean COV derived from M02 (that has a relatively stable orbit), shown in red, confirm the interannual variability.

The COV mean yearly frequency is of about 0.01%, but it varies from about 0.03 ± 0.02‰ in February up to over 0.31 ± 0.11‰ in September. The monthly variability (monthly standard deviation) is largest for July (0.15‰) and October (0.13‰), and smallest in February and March (0.02‰).

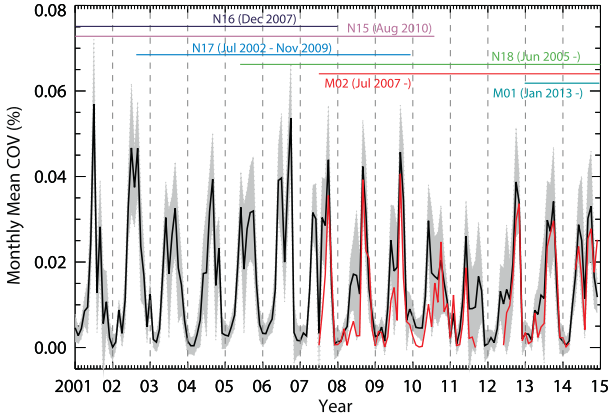

Fig. 7. Monthly mean (black) and standard deviation (shaded) COV frequency (%) based on all satellites overpassing the Mediterranean during the period 2001–2014 for the area [28–48°N, 10°W–40°E]. Red curve is the monthly mean daily COV frequency based on M02 only. Horizontal lines indicate the period where AMSU-B/MHS data were available for each satellite. (For interpretation of the references to colour in this figure legend, the reader is referred to the web version of this article.)

Fig. 8 shows the spatial distribution of the seasonal COV frequency for each year in the period 2005–2008. It was found that the interannual variability is large at all seasons (Fig. 8). In winter (DJF; Fig. 8a–d) COV is predominantly found over the Mediterranean Sea, however COVs median frequency in 2005 (0.14‰) was roughly 60% larger compared to 2006–2008 (median ranging from 0.07–0.09‰).

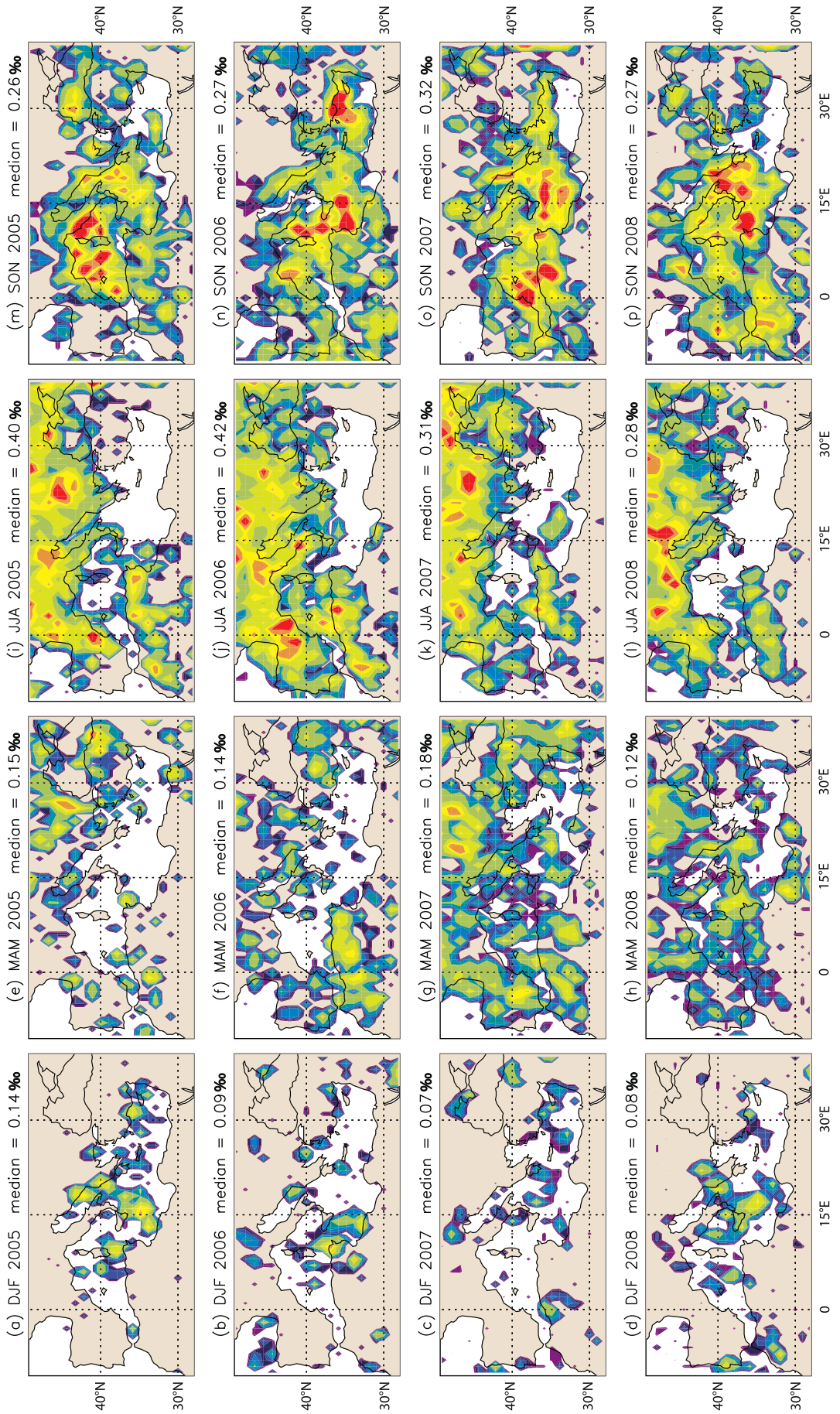

Fig. 8. Interannual variability of COV occurrences by season: (a)-(d) DJF, (e)-(h) MAM, (i)-(l) JJA, and (m)-(p) SON, starting with 2005 (top row) until 2008 (bottom row).

The spatial distribution varies considerably as well, with COV spread in all areas of the Mediterranean Sea in 2005, mainly over the western Mediterranean in 2006, mostly over the eastern side in 2007, and concentrated in the western and central Mediterranean in 2008; the preferred locations, found in all years were around the Italian Peninsula and the coast of Turkey.

MAM is the season that showed the largest spatial interannual variability (Fig. 8e–h): in 2005 and 2006, COV was mainly found over land, whereas in 2007 and 2008 COV was found over both land and sea. The median frequency was comparable among the years, with the lowest value in 2008 (0.12‰) and the highest in 2007 (0.18‰). In this season, COV was consistently found only to the west and south of the Black Sea, in coastal areas in the Adriatic, and over the Atlas Mountains. There was large variability elsewhere. The winter and spring variability are particularly meaningful over the Levant area, as the rainy season is chiefly concentrated from October through May: In most years the rate of occurrence is zero or near zero but in 2007 the frequency attained up to 1.1‰ (90th percentile).

In JJA (Fig. 8i–l), the areas with the largest range in frequency variability were found over Turkey (0–1.5‰) and the western Mediterranean Sea (0– > 2.1‰). Other remarkable variability spots are the Pyrenees, and coastal areas of Portugal and Algeria. The median frequency was larger in 2005 and 2006 (0.40 and 0.42%, respectively) than in 2007 and 2008 (0.31 and 0.28‰, respectively).

Finally, in SON, the interannual variability is strongest along the Turkish coast and eastern Mediterranean Sea, where the frequencies can vary between sporadic occurrences (e.g., in 2005 and 2008; Fig. 8m, p) up to frequencies above the 98th percentile (2006, Fig. 8n). There is also noticeable variability around the Italian Peninsula: while frequencies are generally high around this region, the location of maximum occurrence is variable, for example, it was found largely between the Balearic Islands and the coast of Central Italy including on the Tyrrhenian Sea east of Sardinia in 2005, Southern Mediterranean from the eastern Tunisian coast to the south of Sicily in 2006, south of Italy covering central Mediterranean Sea in 2007 and finally, around Cap Bon Peninsula in Tunisia and in the Strait of Sicily, in the Ionian Sea and on the coast of Albania and Greece on the Adriatic Sea, in 2008. The median value in this season however is comparable in all years, ranging from 0.26–0.32‰.

The interannual variability of COV frequency has good qualitative agreement with that found for overshooting tops by Bedka (2011). The seasonal interannual spatial variability of COV in spring, summer and autumn mimics to a great extent that of DC (not shown). During these seasons, about half of DC events are associated with the presence of an upper-level trough (Funatsu et al., 2008). This supports the notion that COV variability is also strongly linked with the interannual variability of upper-level troughs and the associated (surface) synoptic circulations (Altaratz et al., 2003; Dayan et al., 2015; Raveh-Rubin and Wernli, 2015; Raveh-Rubin and Flaounas, 2017).

4.3. Diurnal variability

The multiple AMSU-B daily overpasses of different platforms was exploited in order to examine whether a diurnal signal of COV can be assessed. Fig. 9 shows the average number of grid points with a valid measurement (i.e., not a missing value) over the domain, considering the period of 2005–2008: For each hour, each $0.2^\circ \times 0.2^\circ$ grid point with a valid value was counted then averaged over the entire domain. As discussed in Section 2.2 the number of valid grid points is larger in the northern part of the domain as the orbits often overlap, while in the southern part there could be gaps between orbits. It is clear from Figs. 1 and 9 that the number of overpasses is irregularly distributed with some hours that are heavily under-sampled, e.g., 07–08 LT, 18–19 LT and 23–00 LT. The results presented here must thus be taken with caution.

Fig. 10 shows the spatial and seasonal distribution of the preferential 6-h interval of COV occurrence. There is overall a large spatial variability on the hour of maximum occurrence. It is however noticeable that from winter to summer, COV is mostly found in the afternoon, after 15 LT (predominance of orange spots on Fig. 10a–c). In SON (Fig. 10d) COV is found predominantly over the sea (cf. Fig. 6d), though a preferential time window does not appear clearly. For this season, analysis of narrower time bins (not shown) suggests a slight preference for night occurrences (00–03 LT) or afternoon (12–18 LT).

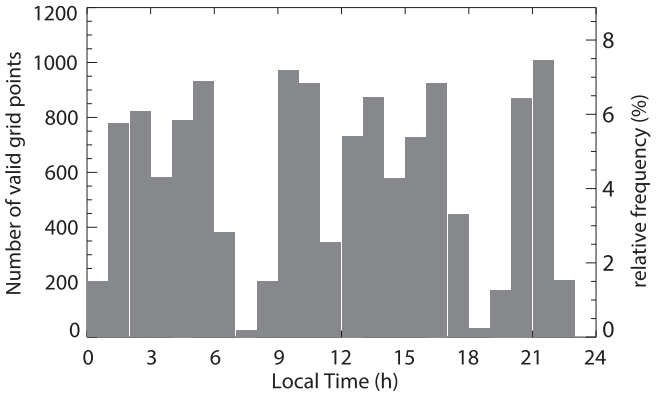

Fig. 9. Mean hourly number of valid grid points (i.e., grid points with an actual measurement) over the domain [28°–48°N; 10°W–40°E], for the period 2005–2008. The right-hand y-axis corresponds to the percentage of mean hourly number of valid grid points (over the entire domain) relative to the average daily total number of grid points over the period.

Fig. 11a and b show the diurnal evolution of COV occurrences over land and sea, respectively. In order to mitigate the sampling bias (irregular diurnal coverage), a three-hour running mean of the COV occurrences was performed. A diurnal pattern is well marked in summer over land (Fig. 11a, red line), with low, nearly constant frequency of about 0.2‰ during the night and morning (between 00 and 12 LT), and net increase in COV frequency after noon reaching around 0.8‰ at 15 LT, and decreasing late evening. The same pattern, though with smaller amplitude (minimum of ~0.1‰ and maximum of ~0.4‰, is observed in the spring (MAM; Fig. 11a, blue line). The maximum occurrence is found near 15 LT, however in both JJA and MAM seasons the minimum at 18 LT may be well an artifact of the low sampling (low number of overpasses) at this time of the day.

Over sea during SON, COV shows several peaks (Fig. 11b). The greatest one around 15 LT is in phase with the diurnal cycle of COV over land suggesting a link between the two, as during this season COV occurrences are typically found near coastal areas (Fig. 6d). This is in line with results of Hamada et al. (2014) who found that in some coastal regions such as the Bay of Bengal and along the western coast of tropical Africa, the diurnal variations of extreme rainfall occurrences are almost in phase with the adjacent land area. The second peak is around 06 LT. Such peak has been observed for rain over oceans (Kikuchi and Wang, 2008). Several causes can explain such peak: the propagation of continental thunderstorms offshore (Yang and Slingo, 2001), the propagation of convective gravity waves that trigger deep convection over the sea (Lac et al., 2002), or the nighttime cooling of the upper-troposphere that leads to destabilization of the maritime air column (Churchill and Houze, 1991).

The local time where COV frequency is largest (15 LT over land and coastal areas) is slightly shifted to later compared to the maximum of convective activity found by Barthlott et al. (2016) for Corsica, but is in good agreement with analysis of OTs detected in the Mediterranean between March–August using infrared-based observations (Bedka, 2011). The local time with least COV occurrences was found around the same time as Bedka (2011), between 07 and 09 LT, but it is necessary to point out that this coincides with heavy under-sampling by AMSU-B. Over the sea, the results for COV did not show preference of occurrences at night, but DC show a slight preference for night-time

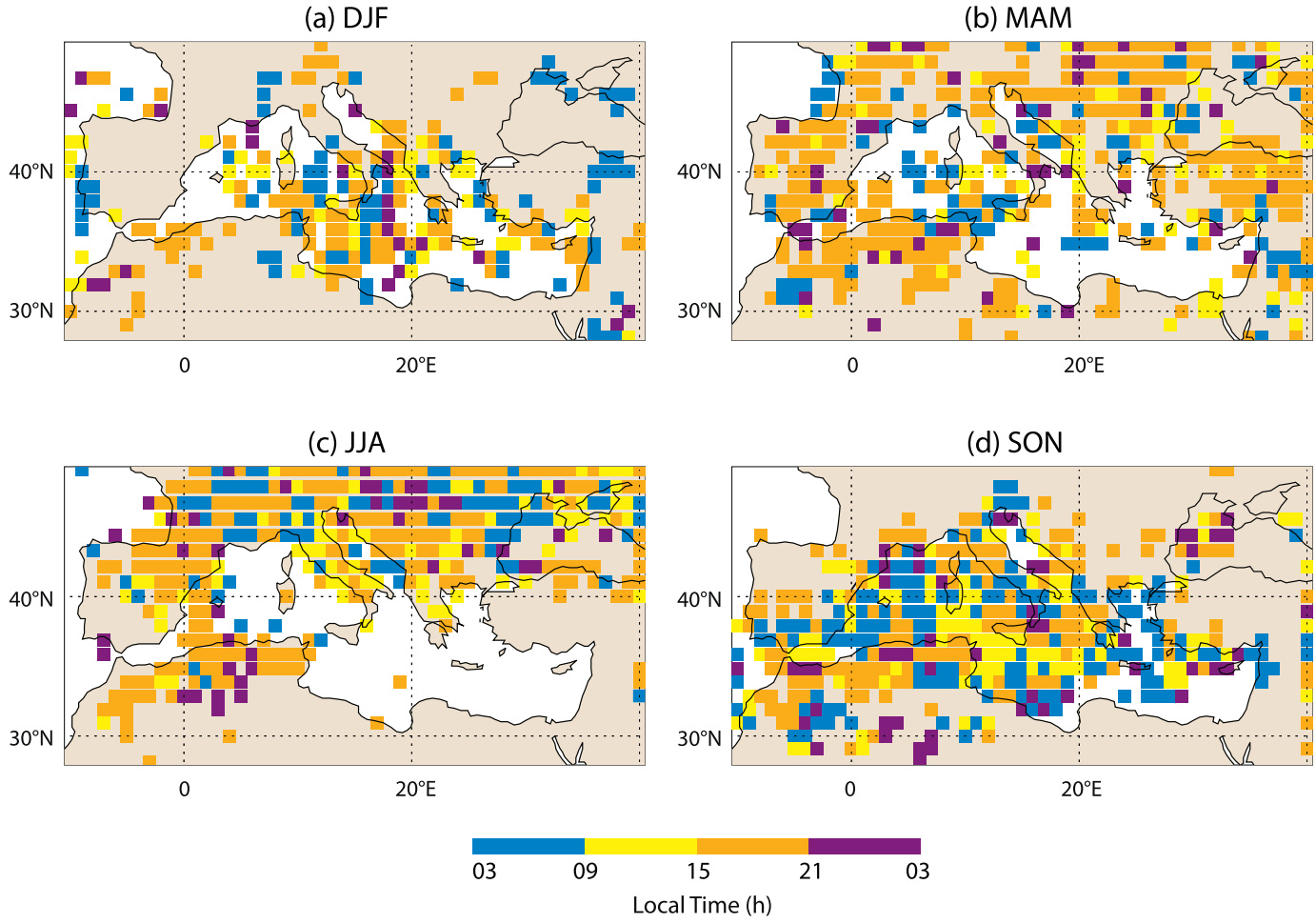

Fig. 10. Most frequent hour of COV occurrences (2005–2008) for (a) DJF, (b) MAM, (c) JJA, and (d) SON. Only grid points where occurrences are larger than the median relative frequency are shown.

occurrence in spring and summer (not shown), as also found by infrared-based observations (Bedka, 2011; Melani et al., 2013), and observed over tropical oceanic areas (Kikuchi and Wang, 2008; Hamada et al., 2014).

The COV maximum found in the afternoon over land is a manifestation of the diurnal cycle of continental convection (e.g., Petrova et al., 2014; Hamada et al., 2014; Wu et al., 2015; Rysman et al., 2016c). The latter is explained by the variation of surface fluxes with the solar insolation. This leads to the daytime development of the planetary boundary layer with a shallow convection in the morning,

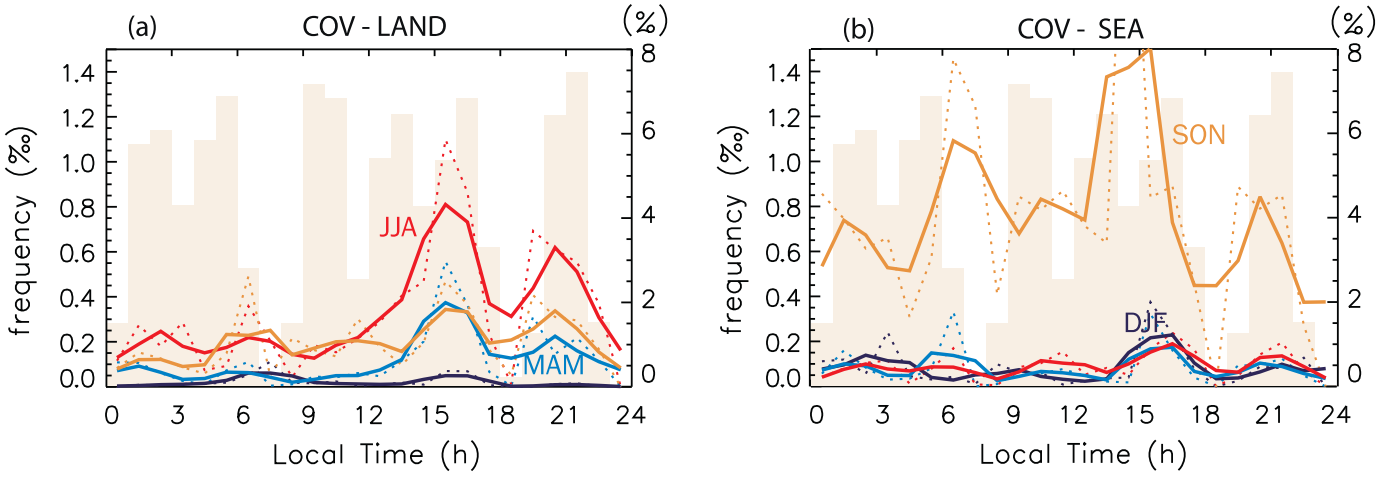

Fig. 11. Mean seasonal hourly (dotted) and 3-h running mean (solid) diurnal evolution of COV over (a) land and (b) sea, for the period of 2005–2008. December–February is shown in dark blue, March–May in blue, June–August in red, and September–November in dark yellow. The light yellow bars shown in the background and its corresponding right-hand side y-axis corresponds to the percentage of mean hourly number of valid grid points (over the entire domain) relative to the average daily total number of grid points over the period as in Fig. 9. (For interpretation of the references to colour in this figure legend, the reader is referred to the web version of this article.)

followed by a gradual onset of deeper convection, with precipitation peaking in the late afternoon to early evening. This general picture is however modulated at regional scale by local effects such as orography and mesoscale circulations. In particular, orography plays a crucial role in the initiation and maintenance of intense storms in the Mediterranean, by both forcing mesoscale circulations and by producing direct lifting of moist surface air parcels against its slopes (Kotroni and Lagouvardos, 2008; Dayan et al., 2015; Raveh-Rubin and Wernli, 2015; Scheffkencht et al., 2017).

5. Summary and conclusions

The major contributions of this work are (i) the microphysical characterization of COV type clouds compared to DC (confirming that COV is a distinctive subset within DC clouds), and (ii) the all-seasons documentation of COV spatio-temporal distribution in the Mediterranean region, based exclusively on microwave observations. The detection of deep convective areas using microwave measurements is achieved using the direct, simple methodology developed by Hong et al. (2005). Their methodology, originally introduced for the tropical region, had been shown to detect clouds with high ice loading content reaching altitudes of 8–9 km in the Mediterranean region by Rysman et al. (2016a) for two case studies.

The main findings of the present work are highlighted below:

1. Convective overshooting can be detected in the Mediterranean region by means of microwave data from AMSU-B using a criterion first proposed for the tropical region by Hong et al. (2005). The COV event observed by both MHS (on N18) and CloudSat shown in Fig. 2 provides an example of the validity of the criterion over the Mediterranean. Furthermore, analysis of the ice cloud height vs tropopause height between 2006 and 2015 over the Mediterranean region indicated that 67% of detected COV cases using the above criterion cross the tropopause, while 78% (82%) are < 1 km (< 2 km) from the tropopause.
2. Analysis of the vertical structure of cloud microphysics of DC (without COV tops) and COV confirm that the latter - as detected using Hong et al. (2005) criterion - are a singular subset of deep convective clouds in the Mediterranean region. COVs present a density of frozen hydrometeors that peak higher in the atmosphere and with large hydrometeors being able to reach 2 km higher compared to DC only clouds (Fig. 3).
3. The temporal evolution of the COV/DC ratio follows that of $\Delta\Theta_{e(1000–300hPa)}$ and of precipitable water (Fig. 4), suggesting that moisture supply and convective instability are underlying factors that enable the transition from DC to COV. The COV/DC ratio follows a seasonal spatial distribution that follows the COV distribution, but with maxima located more to the south (Fig. 5a–c). The median values increase from around 12% in spring to around 20% in summer, and decreasing to about 14% in autumn. It is thus in the summer months that the likelihood of COV occurrence is the greatest in the western and central Mediterranean. In the eastern and southeastern Mediterranean it is in autumn that the proportion COV/DC is the highest, reaching around 20%.
4. COV occur all year long, and are found over both land and sea. COV show a seasonal “migration” from land to sea, with the highest frequencies mostly over land in summer and over sea in autumn (Figs. 6 and 11). It is also remarkable that in winter COV occurrences are found almost exclusively over the sea (Fig. 6a, blue lines in Fig. 10a, b).
5. The interannual variability is very marked in all seasons (Figs. 7 and 8). The largest variability was found for MAM (Fig. 8e–h) when the spatial variability of COV occurrences was found to be highly heterogeneous from year to year. In all seasons, the largest variability was found in the eastern side of the basin, with large frequency fluctuations near the coast of Turkey and the Levant area.
6. There is a net preference for COV occurrence in the afternoon (predominance of orange in Fig. 10, pointing to a time window of 15–21 LT, and Fig. 11 showing larger occurrences in the afternoon particularly over land), though COV can appear at any time (Figs. 10 and 11). These afternoon occurrences in the warm months are closely tied to the diurnal evolution of surface fluxes.

The limitations of the present work are acknowledged as well: Previous studies have pointed out a problem of scan-dependent bias in AMSU-B measurements (e.g., Buehler et al. (2005) and John et al. (2013)) that can be very large depending on the AMSU-B carrying platform, channel and scan position. No scan asymmetry correction was applied to the data before analysis, however the fact that the above presented results do not show aberrant spatial or temporal patterns suggest that the impact of scan asymmetries - and that of N15 channel 4 asymmetries in particular - is limited on the overall analysis. Another issue concerns the detection of deep convection over frozen/snowy land surfaces under clear sky. Under these conditions the rate of false positives for DC was found to be excessively large; the false positives for COV, however, remain low, under 7% for the coldest months, and are found mostly over high topography. Finally, the diurnal sampling by AMSU/MHS carrying platforms has three severe under-sampling slots: between 07 and 08 LT, 18–19 LT, and 23–00 LT (only the latter has actually no coverage). This limits the identification of a diurnal cycle considering relatively broad time ranges.

The COV spatio-temporal distribution shown in the present study may be used as a guide for validation of regional models as to the location and frequency of extreme events in the Mediterranean as was done for example for moderate precipitation and deep convective events by Claud et al. (2012). A comparison between these AMSU-derived products and other two independent data sets specially focused over the Mediterranean Sea was performed by Alhammoud et al. (2014). The latter is of particular importance given the scarce in-situ measurements over the sea, which makes satellite data virtually the only source of widespread observations over maritime areas. In addition, coastal areas that are often affected by extreme weather events are also well resolved in the presented analysis.

AMSU-B/MHS data is now available for over 15 years, and a DC and COV climatology is now available for the whole of mid-latitudes. In addition to support for regional model validation, it could be interesting to relate the COV diagnostics with other proxies; for example, one of hail, recently proposed by Ferraro et al. (2015) for the USA and that also makes use of AMSU. Another interesting lead is to compare COV occurrences to those of lightning, as clouds with larger ice content in the upper troposphere have larger probability of lighting activity (Galanaki et al., 2016). The launch of the Global Precipitation Measurement (GPM) Mission (Hou et al., 2014) in 2014 constitutes an additional opportunity to observe precipitation characteristics and cloud development in the Mediterranean region by means of microwave-sensed data. GPM is equipped with the Dual-frequency Precipitation Radar (besides the advanced GPM Microwave Imager), that allows to carry out analyses of the vertical structure of the convective clouds in the Mediterranean area, as done for example by Marra et al. (2017). While the GPM data capabilities were explored to characterize the structure of an exceptionally violent hailstorm, they also demonstrated how a synergistic use of GPM, MHS, MSG SEVIRI images and ground-based radar data can provide a refined spatio-temporal description of a rapidly developing storm. Besides AMSU/MHS and GPM, the conical scanning Special Sensor Microwave Imager/Sounder (SSMIS) is equipped with 24-channel, 21-frequency, linearly polarized passive microwave radiometer system, including three high frequency channels in the 183.3 GHz water vapor absorption band. The instrument is flown on board the United States Air Force Defense Meteorological Satellite Program (DMSP) F-16, F-17, F-18 and F-19 satellites, which became operational in November 2005, March 2008 March 2016 and May 2016, respectively (https://www.ngdc.noaa.gov/docucomp/page?

xml=NOAA/NESDIS/NCDC/Geoportal/iso/xml/C00827.xml&view=getDataView&header=none). GPM and SSMIS thus provide a further layer of microwave information for cross-comparison with the present study that can close the gaps in the daily coverage that could not be addressed solely by AMSU-carrying platforms, including obtaining a detailed assessment of physical mechanisms leading to the formation and development of COV, and the main factor influencing their genesis.

Acknowledgments

This work was supported by the Direction Générale de l'Armement (DGA) within the PRECIP-CLOUD project, by the French ANR-14-CE01-0014 MUSIC and ANR-12-SENV-0001 REMEMBER projects, and by the Earth2 observe project (funding from the European Union's Framework Programme under grant agreement number 603608). AMSU/MHS data are available at NOAA's Comprehensive Large Array Data Stewardship System. Data set: TOVS. Dataset name format is: NSS.(AMBX|MHSX).(N*|M2). Dyyddd, where yy = year (05 through 08), ddd is the Julian day (001 through 365 or 366); example: NSS.AMBX.NK.D05333.S0133.E0317.B3922324.GC. In this work, AMSU raw data and DARDAR_CLOUD product were obtained with support from the INSU-CNES French Mixed Service Unit ICARE/climserv/AERIS. The authors acknowledge Météo-France for supplying the data and the HyMeX database teams (ESPRI/IPSL and SEDOO/Observatoire Midi-Pyrénées) for their help in accessing the data. We heartily thank three anonymous reviewers for their valuable suggestions and criticism.

References

Adler, R.F., Markus, M.J., Fenn, D.D., 1985. Detection of severe Midwest thunderstorms using geosynchronous satellite data. Mon. Weather Rev. 51, 769–781.

Alhammoud, B., Claud, C., Funatsu, B.M., Béranger, K., Chaboureau, J.-P., 2014. Patterns of precipitation and convection occurrence over the Mediterranean basin derived from a decade of satellite observations. Atmosphere 5, 370–398. http://dx.doi.org/10.3390/atmos5020370.

Alpert, P., Tzidulko, M., Izigsohn, D., 1999. A shallow short-lived meso-beta cyclone over the gulf of Antalya, eastern Mediterranean. Tellus 51A, 249–262.

Altaratz, O., Levin, Z., Yair, Y., Ziv, B., 2003. Lightning activity over land and sea on the eastern coast of the Mediterranean. Mon. Weather Rev. 131, 2060–2070.

Barthlott, C., Kirshbaum, D.J., 2013. Sensitivity of deep convection to terrain forcing over Mediterranean islands. Q. J. R. Meteorol. Soc. 139, 1762–1779. http://dx.doi.org/10.1002/qj.2089.

Barthlott, C., Adler, B., Kalthoff, N., Handwerker, J., Kohler, M., Wieser, A., 2016. The role of Corsica in initiating nocturnal offshore convection. Q. J. Roy. Meteor. Soc. 142, 222–237. http://dx.doi.org/10.1002/qj2415.

Bedka, K.M., 2011. Overshooting cloud top detections using MSG SEVIRI infrared brightness temperatures and their relationship to severe weather over Europe. Atmos. Res. 99, 175–189. http://dx.doi.org/10.1016/j.atmosres.2010.10.001.

Bennartz, R., 2000. Optimal convolution of AMSU-B to AMSU-A. J. Atmos. Ocean. Technol. 17, 1215–1225. http://dx.doi.org/10.1175/1520-0426(2000)017<1215:OCOABT>2.0.CO;2.

Brunner, J.C., Ackerman, S.A., Bachmeir, A.S., Rabin, R.M., 2007. A quantitative analysis of the enhanced-V feature in relation to severe weather. Weather Forecast. 22, 853–872. http://dx.doi.org/10.1175/WAF1022.1.

Buehler, S.A., Kuvatov, M., John, V.O., 2005. Scan asymmetries in AMSU-B data. Geophys. Res. Lett. 32, L24810. http://dx.doi.org/10.1029/2005GL024747.

Buehler, S.A., Kuvatov, M., John, V.O., Milz, M., Soden, B.J., Jackson, D.L., Notholt, J., 2008. An upper tropospheric humidity data set from operational satellite microwave data. J. Geophys. Res. 113, D14110. http://dx.doi.org/10.1029/2007JD009314.

Campins, J., Genovés, A., Picornell, M.A., Jansà, A., 2011. Climatology of Mediterranean cyclones using the ERA-40 dataset. Int. J. Climatol. 31, 1596–1614. http://dx.doi.org/10.1002/joc.2183.

Chaboureau, J.-P., Nuissier, O., Claud, C., 2012. Verification of ensemble forecasts of Mediterranean high-impact weather events against satellite observations. Nat. Hazards Earth Syst. Sci. 12, 2449–2462. http://dx.doi.org/10.5194/nhess-12-2449-2012.

Christian, H., et al., 2003. Global frequency and distribution of lighting as observed from space by the Optial Transient Detector. J. Geophys. Res. 108. http://dx.doi.org/10.1029/2002JD002347.

Chung, E.S., Soden, B.J., John, V.O., 2013. Intercalibrating microwave satellite observations for monitoring long-term variations in upper- and midtropospheric water vapor. J. Atmos. Ocean. Technol. 30, 2303–2319. http://dx.doi.org/10.1175/JTECH-D-13-00001.1.

Churchill, D.D., Houze Jr., R.A., 1991. Effects of radiation and turbulence on the diabatic heating and water budget of the stratiform region of a tropical cloud cluster. J. Atmos. Sci. 48, 903–922.

Claud, C., Alhammoud, B., Funatsu, B.M., Brossier, C.L., Chaboureau, J.-P., Béranger, K., Drobinski, P., 2012. A high resolution climatology of precipitation and deep convection over the Mediterranean region from operational satellite microwave data: development and application to the evaluation of model uncertainties. Nat. Hazards Earth Syst. Sci. 12, 785–798. http://dx.doi.org/10.5194/nhess-12-785-798.

Cohuet, J.B., Romero, R., Homar, V., Ducrocq, V., Ramis, C., 2011. Initiation of a severe thunderstorm over the Mediterranean Sea. Atmos. Res. 100, 603–620. http://dx.doi.org/10.1016/j.atmosres.2010.11.002.

Dauhut, T., Chaboureau, J.-P., Escobar, J., Mascart, P., 2015. Large-eddy simulations of Hector the convector making the stratosphere wetter. Atmos. Sci. Lett. 16, 135–140. http://dx.doi.org/10.1002/asl2.534.

Dayan, U., Nissen, K.M., Ulbrich, U., 2015. Review article: atmospheric conditions inducing extreme precipitation over the Eastern and Western Mediterranean. Nat. Hazards Earth Syst. Sci. 15, 2525–2544. http://dx.doi.org/10.5194/nhess-15-2525-2544.

Dee, D.P., Uppala, S.M., Simmons, A.J., Berrisford, P., Poli, P., Kobayashi, S., Andrae, U., Balmaseda, M.A., Balsamo, G., Bauer, P., Bechtold, P., Beljaars, A.C.M., van de Berg, L., Bidlot, J., Bormann, N., Delsol, C., Dragani, R., Fuentes, M., Geer, A.J., Haimberger, L., Healy, S.B., Hersbach, H., Hólm, E.V., Isaksen, L., Kållberg, P., Köhler, M., Matricardi, M., McNally, A.P., Monge-Sanz, B.M., Morcrette, J.-J., Park, B.-K., Peubey, C., de Rosnay, P., Tavolato, C., Thépaut, J.-N., Vitart, F., 2011. The ERA-interim reanalysis: configuration and performance of the data assimilation system. Q. J. R. Meteorol. Soc. 137, 553–597. http://dx.doi.org/10.1002/qj.828.

Delanoë, J., Hogan, R.J., 2008. A variational scheme for retrieving ice cloud properties from combined radar, lidar, and infrared radiometer. J. Geophys. Res. 113, D07204. http://dx.doi.org/10.1029/2007JD009000.

Delanoë, J., Hogan, R.J., 2010. Combined CloudSat-CALIPSO-MODIS retrievals of the properties of ice clouds. J. Geophys. Res. 115, D00H29. http://dx.doi.org/10.1029/2009JD012346.

Ferraro, R., Beauchamp, J., Cecil, D., Heymsfield, G., 2015. A prototype hail detection algorithm and hail climatology developed with the Advanced Microwave Sounding Unit (AMSU). Atmos. Res. 163, 24–35. http://dx.doi.org/10.1016/j.atmosres.2014.08.010.

Flaounas, E., Raveh-Rubin, S., Wernli, H., Drobinski, P., Bastin, S., 2015. The dynamical structure of intense Mediterranean cyclones. Clim. Dyn. 44, 2411–2427. http://dx.doi.org/10.1007/s00382-014-2330-2.

Funatsu, B.M., Claud, C., Chaboureau, J.-P., 2007. Potential of Advanced Microwave Sounding Unit to identify precipitating systems and associated upper-level features in the Mediterranean region: case studies. J. Geophys. Res. 112, D17113. http://dx.doi.org/10.1029/2006JD008297.

Funatsu, B.M., Claud, C., Chaboureau, J.-P., 2008. A 6-year AMSU-based climatology of upper-level troughs and associated precipitation distribution in the Mediterranean region. J. Geophsy. Res. 113, D15120. http://dx.doi.org/10.1029/2008JD009918.

Funatsu, B.M., Claud, C., Chaboureau, J.-P., 2009. Comparison between the large-scale environments of moderate and intense precipitating systems in the Mediterranean region. Mon. Weather Rev. 137, 3933–3959. http://dx.doi.org/10.1175/2009MWR2922.1.

Galanaki, E., Flaounas, E., Kotroni, V., Lagouvardos, K., Argiriou, A., 2016. Lightning activity in the Mediterranean: quantification of cyclones contribution and relation to their intensity. Atmos. Sci. Lett. 17 (9), 510–516. http://dx.doi.org/10.1002/asl685.

Goldberg, M., Crosby, D.S., Zhou, L., 2001. The limb adjustment of AMSU-A observations: methodology and validation. J. Appl. Meteorol. 40, 70–83.

Greenwald, T.J., Christopher, S.A., 2002. Effect of cold clouds on satellite measurements near 183 GHz. J. Geophys. Res. 107 (D13). http://dx.doi.org/10.1029/2000JD000258. AAC 3-1–AAC 3-8.

Hamada, A., Murayama, Y., Takayabu, Y.N., 2014. Regional characteristics of extreme rainfall extracted from TRMM PR measurements. J. Clim. 27, 8151–8169. http://dx.doi.org/10.1175/JCLI-D-14-00107.1.

Hassim, M., Lane, T., 2010. A model study on the influence of overshooting convection on TTL water vapour. Atmos. Chem. Phys. 10, 9833–9849. http://dx.doi.org/10.5194/acp-10-9833-2010.

Holt, M., Hardaker, P., McLelland, G., 2001. A lightning climatology for Europe and the UK, 1990–99. Weather 56, 290–296.

Holton, J., Gettelman, A., 2001. Horizontal transport and dehydration of the stratosphere. Geophys. Res. Lett. 28, 2799–2802. http://dx.doi.org/10.1029/2001GL013148.

Hong, G., Heygster, G., Miao, J., Kunzi, K., 2005. Detection of tropical deep convective clouds from AMSU-B water vapor channels measurements. J. Geophys. Res. 110, D05205. http://dx.doi.org/10.1029/JD004949.

Hou, A.Y., et al., 2014. The global precipitation measurement mission. Bull. Am. Meteor. Soc. 95, 701–722. http://dx.doi.org/10.1175/BAMS-D-13-00164.1.

Iwasaki, S., Shibata, T., Nakamoto, J., Okamoto, H., Ishimoto, H., Kubota, H., 2010. Characteristics of deep convection measured by using the A-train constellation. J. Geophys. Res. 115, D06207. http://dx.doi.org/10.1029/2009JD013000.

Jansà, A., Genovés, A., Picornell, M.A., Campins, J., Riosalido, R., Carretero, O., 2001. Western Mediterranean cyclones and heavy-rain. Part 2: statistical approach. Meteorol. Appl. 8 (1), 43–56.

John, V.O., Holl, G., Atkinson, N., Buehler, S.A., 2013. Monitoring scan asymmetry of microwave humidity sounding channels using simultaneous all angle collocations (SAACs). J. Geophys. Res. 118, 1536–1545. http://dx.doi.org/10.1002/jgrd.50154.

Kahana, R., Ziv, B., Enzel, Y., Dayan, U., 2002. Synoptic climatology of major floods in the Negev desert. Israel. Int.J. Climatol 22, 867–882. http://dx.doi.org/10.1002/joc.766.

Kikuchi, K., Wang, B., 2008. Diurnal precipitation regimes in the global tropics. J. Clim. 21, 2680–2696. http://dx.doi.org/10.1175/2007JCLI2051.1.

Kotroni, V., Lagouvardos, K., 2008. Lightning occurrence in relation with elevation, terrain slope and vegetation cover in the Mediterranean J. Geophys. Res. 113, D21118. http://dx.doi.org/10.1029/2008JD010605.

Kotroni, V., Lagouvardos, K., 2016. Lightning in the Mediterranean and its relation with

sea-surface temperature. Environ. Res. Lett. 11, 034006. http://dx.doi.org/10.1088/1748-9326/11/3/034006.
Kotroni, V., Lagouvardos, K., Defer, E., Dietrich, S., Porcù, F., Medaglia, C.M., Demirtas, M., 2006. The antalya 5 December 2002 storm: observations and model analysis. J. Appl. Meteorol. Climatol. 45, 576–590. http://dx.doi.org/10.1175/JAM2347.1.
Lac, C., Lafore, J., Redelsperger, J., 2002. Role of gravity waves in triggering deep convection during TOGA COARE. J. Atmos. Sci. 59, 1293–1316. http://dx.doi.org/10.1175/1520-0469(2002)059<1293:ROGWIT>2.0.CO;2.
Laviola, S., Moscatello, A., Miglietta, M.M., Cattani, E., Levizzani, V., 2011. Numerical model investigation of two heavy rain events over the Central Mediterranean. J. Hydrometeorol. 12, 634–649. http://dx.doi.org/10.1175/2011JHM1257.1.
Laviola, S., Levizzani, V., Cattani, E., Kidd, C., 2013. The 183-WSL fast rain rate retrieval algorithm. Part II: Validation using ground radar measurements. Atmos. Res. 134, 77–86. http://dx.doi.org/10.1016/j.atmosres.2013.07.013.
Levizzani, V., Pinelli, F., Pasqui, M., Melani, S., Laing, A.G., Carbone, R.E., 2010. A 10-year climatology of warm-season cloud patterns over Europe and the Mediterranean from Meteosat IR observations. Atmos. Res. 97, 555–576. http://dx.doi.org/10.1016/j.atmosres.2010.05.014.
Machado, L.A.T., Lima Jr., W.F.A., Pinto, Osmar, Morales, C.A., 2009. Relationship between cloud-to-ground discharge and penetrative clouds: a multi-channel satellite application. Atmos. Res. 93, 304–309. http://dx.doi.org/10.1016/j.atmosres.2008.10.003.
Mandapaka, P.V., Germann, U., Panziera, L., 2013. Diurnal cycle of precipitation over complex Alpine orography: inferences from high-resolution radar observations. Q. J. R. Meteorol. Soc. 139, 1025–1046. http://dx.doi.org/10.1002/qj.2013.
Marra, A.C., Porcù, F., Baldini, L., Petracca, M., Casella, D., Dietrich, S., Mugnai, A., Sanò, P., Vulpiani, G., Panegrossi, G., 2017. Observational analysis of an exceptionally intense hailstorm over the Mediterranean area: role of the GPM Core Observatory. Atmos. Res. 192, 72–90. http://dx.doi.org/10.1016/j.atmosres.2017.03.019.
Massacand, A.C., Wernli, H., Davies, H.C., 1998. Heavy precipitation on the Alpine southside: an upper-level precursor. Geophys. Res. Lett. 25, 1435–1438. http://dx.doi.org/10.1029/98GL50869.
Matsui, T., Santanello, J., Shi, J.J., Tao, W.-K., Wu, D., Peters-Lidard, C., Kemp, E., Chin, M., Starr, D., Sekiguchi, M., Aires, F., 2014. Introducing multisensor satellite radiance-based evaluation for regional Earth System modeling. J. Geophys. Res. 119, 8450–8475. http://dx.doi.org/10.1002/2013JD021424.
Melani, S., Pasi, F., Gozzini, B., Ortolani, A., 2013. A four year (2007–2010) analysis of long-lasting deep convective systems in the Mediterranean basin. Atmos. Res. 123, 151–166. http://dx.doi.org/10.1016/j.atmosres.2012.09.006.
Nastos, P.T., Kapsomenakis, J., Douvis, K., 2013. Analysis of precipitation extremes based on satellite and high-resolution gridded data set over Mediterranean basin. Atmos. Res. 131, 46–59. http://dx.doi.org/10.1016/j.atmosres.2013.04.009.
Negri, A.J., Adler, R.F., 1981. Relation of satellite-based thunderstorm intensity to radar-estimated rainfall. J. Appl. Meteorol. 20, 288–300.
Petrova, S., Mitzeva, R., Kotroni, V., 2014. Summer-time lightning activity and its relation with precipitation: diurnal variation over maritime, coastal and continental areas. Atmos. Res. 135, 388–396. http://dx.doi.org/10.1016/j.atmosres.2012.10.015.
Proud, S.R., 2015. Analysis of overshooting top detections by Meteosat Second Generation: a 5-year dataset. Q. J. R. Meteorol. Soc. 141, 909–915. http://dx.doi.org/10.1002/qj.2410.
Punge, H.J., Kunz, M., 2016. Hail observations and hailstorm characteristics in Europe: a review. Atmos. Res. 176-177, 159–184. http://dx.doi.org/10.1016/j;atmosres.2016.02.012.
Raveh-Rubin, S., Flaounas, E., 2017. A dynamical link between deep Atlantic extra-tropical cyclones and intense Mediterranean cyclones. Atmos. Sci. Lett. 18 (5), 215–221. http://dx.doi.org/10.1002/asl475.
Raveh-Rubin, S., Wernli, H., 2015. Large-scale wind and precipitation extremes in the Mediterranean: a climatological analysis for 1979–2012. Q. J. R. Meteorol. Soc. 141, 2404–2417. http://dx.doi.org/10.1002/qj.2531.
Reynolds, D.W., 1980. Observations of damaging hailstorms from geosynchronous satellite digital data. Mon. Weather Rev. 108, 337–348.
Rubin, S., Ziv, B., Paldor, N., 2007. Tropical plumes over eastern North Africa as a source of rain in the Middle East. Mon. Weather Rev. 135, 4135–4148. http://dx.doi.org/10.1175/2007MWR1919.1.
Rysman, J.-F., Claud, C., Chaboureau, J.-P., Delanoë, J., Funatsu, B.M., 2016a. Severe convection in the Mediterranean from microwave observations and a convection-permitting model. Q. J. R. Meteorol. Soc. 142, 43–55. http://dx.doi.org/10.1002/qj.2611.
Rysman, J.-F., Berthou, S., Claud, C., Drobinski, P., Chaboureau, J.-P., Delanoë, J., 2016b. Potential of microwave observations for the evaluation of rainfall and convection in a regional climate model in the frame of HyMeX and MED-CORDEX. Clim. Dyn. http://dx.doi.org/10.1007/s00382-016-3203-7.
Rysman, J.F., Lemaître, Y., Moreau, E., 2016c. Spatial and temporal variability of rainfall in the alps–Mediterranean Euroregion. J. Appl. Meteorol. Climatol. 55 (3), 655–671. http://dx.doi.org/10.1175/JAMC-D-15-0095.1.
Rysman, J.-F., Claud, C., Delanoë, J., 2017. Monitoring deep convection and convective overshooting from 60°S to 60°N using MHS: a Cloudsat/CALIPSO-based assessment. IEEE Geosci. Remote Sens. Lett. 14, 159–163. http://dx.doi.org/10.1109/LGRS.2016.2631725.
Saaroni, H., Halfon, N., Ziv, B., Alpert, P., Kutiel, H., 2010. Links between the rainfall regime in Israel and location and intensity of Cyprus lows. Int. J. Climatol. 30, 1014–1025. http://dx.doi.org/10.1002/joc.1912.
Sassen, K., Wang, Z., 2008. Classifying clouds around the globe with the CloudSat radar: 1-year of results. Geophys. Res. Lett. 35, L04805. http://dx.doi.org/10.1029/2007GL032591.
Scheffkencht, P., Richard, E., Lambert, D., 2017. Climatology of heavy precipitation over Corsica in the period 1985–2015. Q. J. R. Meteorol. Soc. http://dx.doi.org/10.1002/qj3140.
Surussawadee, C., Staelin, D.H., 2010. Global precipitation retrievals using the NOAA AMSU millimeter-wave channels: comparisons with rain gauges. J. Appl. Meteorol. Climatol. 49, 124–135. http://dx.doi.org/10.1175/2009JAMC2262.1.
Trigo, I.F., Bigg, G.R., Davies, T.D., 2002. Climatology of cyclogenesis mechanisms in the Mediterranean. Mon. Weather Rev. 130, 549–569. http://dx.doi.org/10.1175/1520-0493(2002)130<0549:COCMIT>2.0.CO;2.
Turato, B., Reale, O., Siccardi, F., 2004. Water vapor sources of the October 2000 piedmont flood. J. Hydrometeorol. 5, 693–712. http://dx.doi.org/10.1175/1525-7541(2004)005<0693:WVSOTO>2.0.CO;2.
Weng, F., Zhao, L., Ferraro, R.R., Poe, G., Li, X., Grody, N.C., 2003. Advanced Microwave Sounding Unit cloud and precipitation algorithms. Radio Sci. 38 (4), 8068. http://dx.doi.org/10.1029/2002RS002679.
Wu, C.M., Lo, M.H., Chen, W.T., Lu, C.T., 2015. The impacts of heterogeneous land surface fluxes on the diurnal cycle precipitation: a framework for improving the GCM representation of land-atmosphere interactions. J. Geophys. Res. 120, 3714–3727. http://dx.doi.org/10.1002/2014JD023030.
Yang, G.-Y., Slingo, J., 2001. The diurnal cycle in the tropics. Mon. Weather Rev. 129, 784–801.
Ziv, B., Dayan, U., Sharon, D., 2005. A mid-winter, tropical extreme flood-producing storm in southern Israel: synoptic scale analysis. Meteorog. Atmos. Phys. 88, 53–63. http://dx.doi.org/10.1007/s00703-003-0054-7.
Ziv, B., Dayan, U., Kushnir, Y., Roth, C., Enzel, Y., 2006. Regional and global atmospheric patterns governing rainfall in the southern Levant. Int. J. Climatol. 6, 55–73. http://dx.doi.org/10.1002/joc.1238.